Chemical Geology 658 (2024) 122120

Contents lists available at ScienceDirect

Chemical Geology

journal homepage: www.elsevier.com/locate/chemgeo

Silicon and oxygen isotope fractionation in a silicified carbonate rock

Michael Tatzel [a,*], Marcus Oelze [b], Daniel A. Frick [c,d], Tommaso Di Rocco [a], Moritz Liesegang [e,f], Maria Stuff [c], Michael Wiedenbeck [c]

[a] Department of Sedimentology and Environmental Geology, Geoscience Center Georg-August-Universität Göttingen, 37077 Göttingen, Germany
[b] Bundesanstalt für Materialforschung und –prüfung, 12489 Berlin, Germany
[c] GFZ German Research Centre for Geosciences, 14473 Potsdam, Germany
[d] Paleoceanography and Marine Geology, Kiel University, 24118 Kiel, Germany
[e] RMS Foundation, Bischmattstrasse 12, 2544 Bettlach, Switzerland
[f] Institut für Geologische Wissenschaften, Freie Universität Berlin, Malteserstrasse. 74–100, 12249 Berlin, Germany

ARTICLE INFO

Editor: Vasileios Mavromatis

Keywords:
Chert
Silicification
Silicon isotopes
Oxygen isotopes
Temperature
Mineral replacement

ABSTRACT

Silicon isotope fractionation during silicification is poorly understood and impedes our ability to decipher paleoenvironmental conditions from Si isotopes in ancient cherts. To investigate isotope fractionation during silica-for-carbonate replacement we analyzed the microscale Si and O isotope composition in different silica phases in a silicified zebra dolostone as well as their bulk $\delta^{18}O$ and $\Delta'^{17}O$ compositions. The subsequent replacement of carbonate layers is mimicked by decreasing $\delta^{18}O$ and $\delta^{30}Si$. The textural relationship and magnitude of Si and O isotope fractionation is best explained by near-quantitative silica precipitation in an open system with finite Si. A Rayleigh model for silicification suggests positive $\varepsilon^{30/28}Si$ during silicification, conforming with predictions for isotope distribution at chemical equilibrium from ab-initio models. Application of the modelled $\varepsilon^{30}Si$-T relationship yields silicification temperatures of approx. 50 °C. To reconcile the $\delta^{18}O_{chert}$ composition with these temperatures, the $\delta^{18}O$ of the fluid must have been between −2.5 and − 4 ‰, compositions for which the quartz phases fall close to the oxygen equilibrium fractionation line in three-isotope space. Diagenetic silica replacement appears to occur in O and Si isotopic equilibrium allowing reconstructions of temperatures of silicification from Si isotopes and derive the $\delta^{18}O$ composition of the fluid – a highly desired value needed for accurate reconstructions of the temperature- and $\delta^{18}O$ histories of the oceans.

1. Introduction

Chert, a near-monomineralic rock made of silica, is resistant to alteration and widely found since the Archean and thus a prime archive of near-surface conditions in deep geological time. Yet, the reconstructions based on stable isotope ratios are ambiguous due to the largely unknown source fluid compositions and the different modes of chert formation, which are likely associated with different isotope fractionation mechanisms. Chert either forms from siliceous sediment during burial diagenesis, i.e. 'sedimentary chert' or by replacement of a precursor rock, i.e. 'replacement chert' (Hesse, 1989; van den Boorn et al., 2007). Sedimentary chert forms from amorphous silica precursors (opal-A) that transform during burial diagenesis to quartz via a metastable silica phase composed of low-cristobalite and low-tridymite (opal-CT) (e.g. Kastner et al., 1977; Williams and Crerar, 1985; Williams et al., 1985). These polymorph transformations are typically fluid-buffered and therefore oxygen isotope ratios ($\delta^{18}O_{chert} = {}^{18/16}O_{sample}/{}^{18/16}O_{V\text{-}SMOW}$ -1) reequilibrate with fluids at elevated temperatures during burial diagenesis (Murata et al., 1977; Yanchilina et al., 2020, 2021; Ibarra et al., 2022). This reduces the leverage of seawater temperatures (T_{SW}) over $\delta^{18}O_{chert}$ and highlights the role of diagenetic temperatures and the prograde T-t path on $\delta^{18}O_{chert}$ (Tatzel et al., 2022). On the bulk rock scale silicon isotope ratios ($\delta^{30}Si = {}^{30/28}Si_{sample}/{}^{30/28}Si_{NBS\ 28}$–1) are less susceptible to post-depositional alteration due to the low Si solubility in most fluids. The low-dissolved silica (dSi) Cenozoic seawater causes drastic dissolution of siliceous sediments during early diagenesis that modify the bulk sediment $\delta^{30}Si$ (Tatzel et al., 2015). Conversely, the high-dSi Precambrian seawater prevented such effects and even lead to inorganic silica precipitation from seawater (Siever, 1992). Thus, Si isotopes in Paleozoic and older sedimentary chert are thought to preserve the original signatures from the amorphous precursor materials (Tatzel et al., 2017, 2020).

* Corresponding author.
E-mail address: michael.tatzel@uni-goettingen.de (M. Tatzel).

https://doi.org/10.1016/j.chemgeo.2024.122120
Received 17 August 2023; Received in revised form 24 April 2024; Accepted 27 April 2024
Available online 29 April 2024

Replacement cherts or silicified rocks can form by precipitation in pore space and by coupled dissolution-precipitation (Putnis and Putnis, 2007). A thin fluid film, ranging from only a few monolayers of water molecules to several hundreds of nanometers thick, and the amorphous precipitates thereof can order over short distances and thereby preserve structural information of the dissolved precursor (Hellmann et al., 2012; Liesegang et al., 2017). Thereby the protolith identity can be documented in remnant minerals, also known as 'ghosts' (Maliva and Siever, 1988, 1989b). In carbonates the replacement process can occur via different mechanisms including the mixing of meteoric and marine waters that leads to silica oversaturation and carbonate undersaturation (Knauth, 1979) or through the decomposition of organic matter that leads to a pH reduction (Siever, 1962; Knoll, 1985). Further, the force of crystallization has been inferred to promote the carbonate-by-quartz replacement process (Maliva and Siever, 1987). Thereby, meso- and microcrystalline quartz forms by direct precipitation (replacement or precipitation in pore space) and not by 'ageing', i.e. diagenetic maturation of a precursor silica phase (Maliva and Siever, 1988).

The high dSi levels in the Precambrian are also thought to lead to silicification in the peritidal zone (Maliva et al., 1989, 2005). The occurrence of different silica phases in silicified rocks appears to be controlled by the structural and chemical properties of the protolith, e.g. carbonate grains are typically replaced by microquartz and less commonly by chalcedony, which forms as void filling cements along with megaquartz (Maliva and Siever, 1989a) and sulfate is replaced by 'length-slow' chalcedony (Folk and Pittman, 1971). Silicified volcaniclastic rocks can also be chemically distinguished from inorganic silica precipitation, namely from the Al-δ^{30}Si relationship (van den Boorn et al., 2007).

When silicification occurs during early diagenesis or telodiagenesis, O- and H- isotopes of quartz can record meteoric conditions (Abruzzese et al., 2005; Bustillo, 2010). Si stable isotopes in silicified rocks are expected to fractionate differently compared to cherts derived from amorphous silica precursors. Si isotopes in silicified Archean rocks are typically isotopically 'heavy', e.g. in silicified volcanogenic sediments in Pilbara (0.1 to 1.1 ‰ δ^{30}Si) (van den Boorn et al., 2007, 2010) and in silicified basalt in Barberton (0.2 to 1.1 ‰ δ^{30}Si) (Abraham et al., 2011). These signatures are explained by ^{30}Si-rich seawater and negative isotopic fractionation ε^{30}Si ($= \alpha^{30}\mathrm{Si}_{\text{chert-fluid}} - 1$) as is typically observed in experiments conducted at low temperature (e.g. Geilert et al., 2014a; Oelze et al., 2014; Oelze et al., 2015; Roerdink et al., 2015) and during rapid precipitation where kinetics dominate the mineral precipitation reaction such as in silica deposits from hydrothermal fluids (Geilert et al., 2014b, 2015). Si isotope fractionation during silicification is only sparsely studied, and available data do not yield a consistent picture, thus still impeding the interpretation of δ^{30}Si in silicified rocks. Large isotopic variations of ca. 6 ‰ on the microscale in silicified corals are explained by Rayleigh distillation in a finite Si reservoir with ε^{30}Si < 0 ‰ (Andrade et al., 2020). Silicified carbonates in a cave were suggested to record a hydrothermally-induced lowering of δ^{30}Si by 3 to 4 ‰ (Pisani et al., 2022).

Here, we investigate Si and O isotope fractionation during carbonate replacement by silica on the microscale in a chert containing a range of silica polymorphs that emerge from its zebra-dolomite protolith. We discuss different possible interpretations and present an open-system fractionation model that suggests preferential incorporation of ^{30}Si during silicification.

2. Materials & methods

2.1. Samples

The silicified dolostone specimen was collected at Koksu (43°39′13.00″N, 69°38′10.97″E) from the base of the Lower Cambrian cherts of the 'Aksai member' in the Malyi Karatau range of Kazakhstan. The up to 20 m thick unit of bedded chert sharply overlies the karsted surface of the 'Berkuty dolostone', a medium- to coarse grained dolostone that formed in shallow water (Heubeck et al., 2013) and that belongs to the lowermost Chulaktau Formation, which is presumably of Lower Cambrian age (Eganov et al., 1986). Cherts at the base of the unit are partly silicified dolostones, some of which are characterized by repeated patterns of chemical and textural variation, referred to as zebra chert. The regularly patterned dolostones likely formed under certain permeability and stress regimes from dolostones that are rich in impurities (Kelka et al., 2017). Dolomite recrystallization results in a wide range of crystal sizes and crystal purity that occur in repeated patterns and reflect their diagenetic origin (e.g., Nielsen et al., 1998; Vandeginste et al., 2005).

Transmitted light microscopy reveals that the zebra chert specimen consists of four parallel, repetitive units with horizontal to subhorizontal orientation: (1) microquartz with minor intergrown cryptoquartz, (2) thin botryoidal chalcedony bands, (3) cryptocrystalline quartz intergrown with fibrous chalcedony, and (4) fibrous chalcedony veins. The fibrous chalcedony intergrown in cryptoquartz (3) appears to have penetrated from the contacting fibrous chalcedony veins (4). All units are cross-cut and slightly displaced by vertical to subvertical veins composed of coarse quartz (5). The textural relationships chronicle the order of their formation (Fig. 1).

The equigranular microquartz bands (1) are composed of up to 20 μm-sized, interlocked quartz crystals with undulose extinction and irregular grain boundaries. This quartz mosaic encloses silicified, irregularly shaped intraclasts (60–300 μm) and euhedral to subhedral ghosts of unknown origin. Both structures contain minor hematite and are rimmed by euhedral apatite crystals most commonly ranging from ~3 to 12 μm. Microquartz bands are covered by a botryoidal layer of ~50 μm thick length-fast, radially fibrous chalcedony (2) with an outward growth direction. These botryoidal chalcedony bands (2) mark the sharp boundary between microquartz bands (1), chalcedony veins (4) below, and cryptocrystalline quartz layers above (3). It is possible that the botryoidal chalcedony formed first on top of the not yet silicified carbonate that subsequently transformed to microquartz. Initial precipitation of botryoidal chalcedony on carbonate surfaces is e.g. observed in the Neoproterozoic Doushantuo Formation where the oxidation of organic matter is thought to have induced early diagenetic precipitation of fibrous silica (Papineau et al., 2021). Botryoidal chalcedony formation in the Precambrian Gunflint Formation is thought to have been either associated with the infiltration of bitumen or coevally with organic matter emplacement (Varkouhi and Papineau, 2023). The cryptocrystalline quartz layers are generally pale brown in plane polarized light due to the presence of abundant hematite and minor pyrite grains (< 5 μm). The thickness of these layers gradually decreases from 2.5 mm to 100 μm towards the top of the section. Rare apatite crystals (< 10 μm) occur randomly throughout the material. Thin interconnected chalcedony veins (< 80 μm wide) protrude from the horizontal chalcedony veins (4) into the cryptocrystalline quartz domains resulting in a peloid-like substructure (Fig. 1e). The transition from cryptocrystalline quartz layers (3) to chalcedony veins (4) is abrupt and lacks any gradual changes of crystal size or texture. Opposing bands of wall-lining chalcedony are composed of parabolic twisted fiber bundles that form the horizontal to subhorizontal veins (4) (Fig. 1g). The inclusion-free fiber bundles radiate towards the center of the veins. Cathodoluminescence analysis reveals that angular quartz succeeds chalcedony in the vein center (4b) (Fig. 2). The fibrous chalcedony bands are sandwiched between cryptocrystalline layers below and botryoidal chalcedony-lined microquartz layers above.

3. Methods

3.1. Silicon isotope analysis by MC fs-LA ICP-MS

Silicon isotope ratios were analyzed using UV femtosecond laser ablation multi-collector inductively coupled plasma mass spectrometry

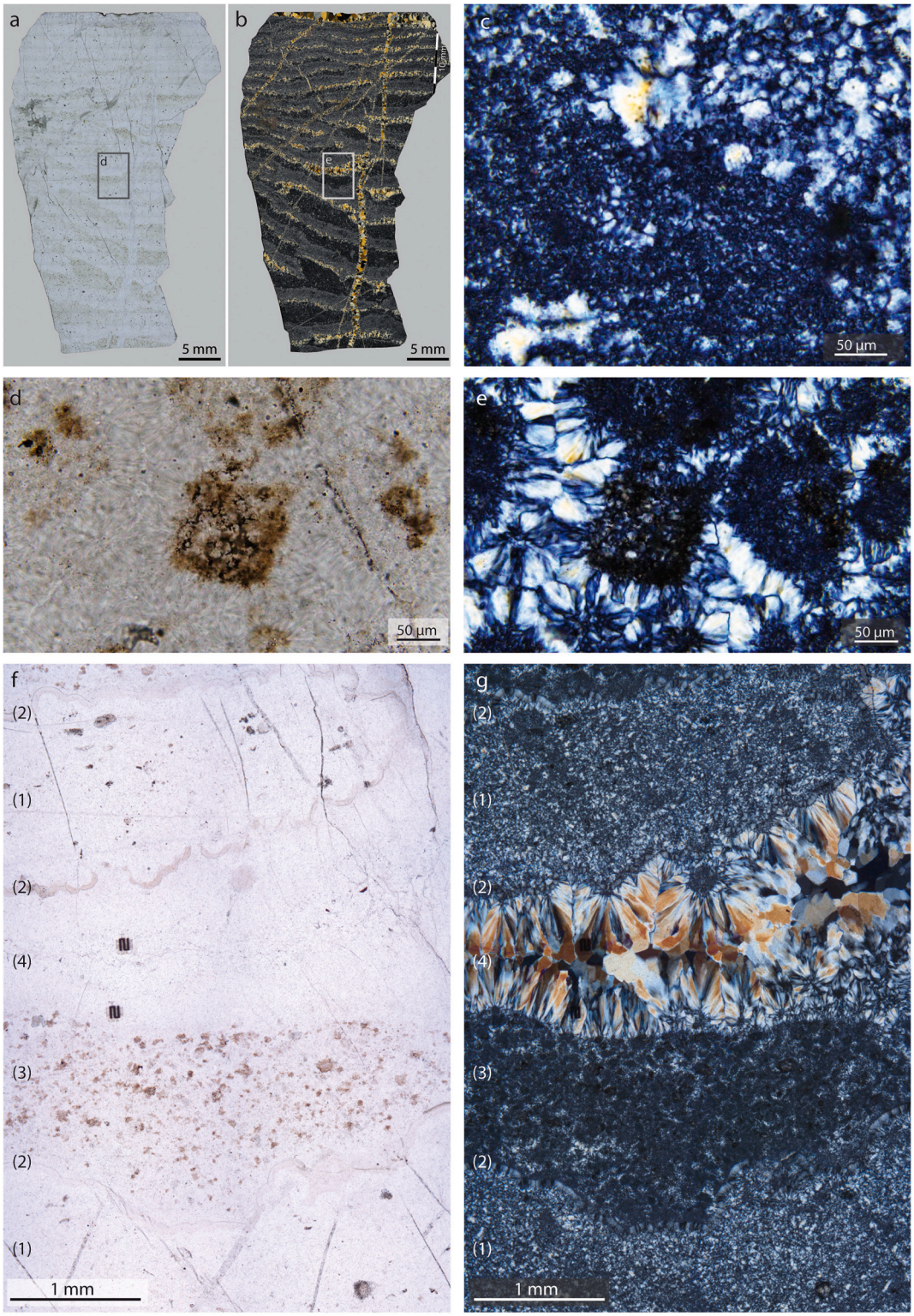

Fig. 1. Microphotographs of the silica-replaced zebra dolomite under plane-polarized (a, d, f) and cross-polarized light (b, c, e, g). a) and b) show the entire thin section of the silicified zebra-dolomite, c) shows a close-up of the microcrystalline quartz with minor intergrown cryptocrystalline quartz, d) and e) show cryptocrystalline quartz with intergrown chalcedony, f and g) show the textural relationship between the different silica phases.The numbers correspond to the order of replacement and to the numbering in the text. Microquartz (1) might have formed before or after botryoidal chalcedony (2) (see main text).

(UV fs LA MC-ICP-MS) at the German Research Centre for Geosciences (GFZ) Potsdam in the Helmholtz Laboratory for the Geochemistry of the Earth Surface (HELGES; von Blanckenburg et al., 2016). A polished thin section (≈ 30 µm) of the sample was mounted into the ablation cell together with epoxy-embedded grains of the bracketing standard NBS 28 (quartz sand), and external quality control materials BHVO-2G (USGS, basalt glass) and IRMM-017 (Si single crystal). The laser beam (196 nm, < 200 fs pulses) was scanned at 40 µm/s over an area of 100 µm^2, ablating an approx. 10 µm thick layer. For small crystals with complex shapes (botryoidal calcedony and most NBS 28 quartz grains), an

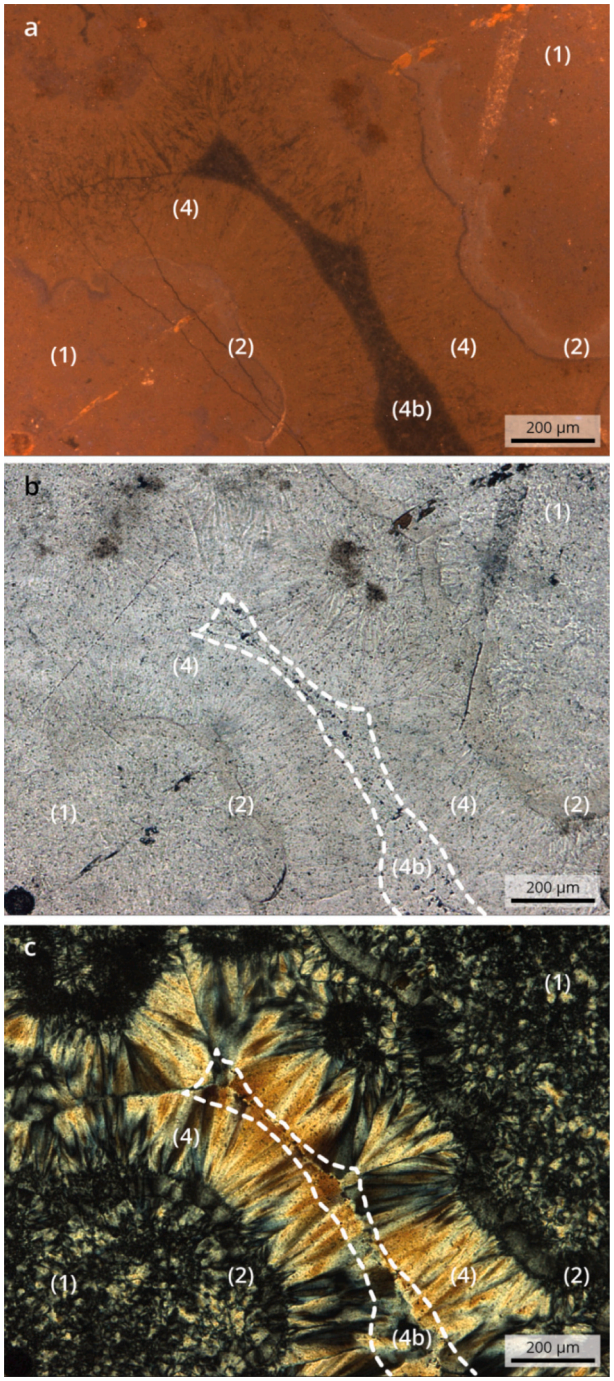

Fig. 2. Angular quartz fill (4b) enclosed in a fibrous chalcedony band (4) that fills the space between botryoidal chalcedony-lined microquartz (1) in cathodoluminescent light (a), plane- (b) and cross-polarized light (c).

equivalent volume was ablated by lasing individually programmed paths. The focusing of the laser beam below the sample surface resulted in crater widths of 18–25 µm and a fluence of 3.6 J/cm^2. Helium was used as carrier gas and was mixed with Ar and H_2O through SIS-spray chamber nebulization of deionized-H_2O before entering the ICP source of the mass spectrometer. The interface was equipped with a Ni Jet sample cone and a Ni H-skimmer cone. The Faraday cups were aligned to resolve interferences from molecular oxides and to record $^{28}Si^+$, $^{29}Si^+$, $^{30}Si^+$, and $^{27}Al^+$ simultaneously as previously in Tatzel et al. (2015). Measurements were done in high resolution mode with a mass-resolving power of 10,350 (m/Δm). Under these analytical conditions, repetition rates of 40 Hz on quartz (sample and NBS 28) yielded mostly between 5 and 7.6 V ^{28}Si using 10^{11} Ω resistors. Intensity matching between samples and alternatingly measured NBS 28 quartz grains was mostly within 20%. BHVO-2G and IRMM-017 were measured at repetition rates of 58.8 Hz and 11.5 Hz to match signal intensities. Each measurement represents the mean of integrated isotope ratios of approx. 80 cycles (each integrated over 1.049 s) corrected for background Si intensities of I(^{28}Si) = 15 mV. Analyses were followed by a 70 s long wash time to remove aerosols produced during analysis. Data evaluation followed the protocol detailed in Schuessler and von Blanckenburg (2014) that includes the screening of time-resolved data. Al concentrations were calibrated using measured $^{27}Al/^{28}Si$ in BHVO-2G assuming an Al/Si mass ratio of 0.31 (GeoReM compiled value; Jochum et al., 2005). Isotope ratios are reported as per mil deviation of isotope ratios relative to NBS 28 (δ-notation). The analytical precision reported is the internal standard error of the mean (2 SE) that was always <0.11 ‰ 2 SE for $\delta^{29}Si$ and < 0.16 ‰ 2 SE for $\delta^{30}Si$ (n = 71). The long-term external reproducibility of the method is 0.15 ‰ on $\delta^{29}Si$ (2 s) and 0.23 ‰ on $\delta^{30}Si$ (2 s) and must be used when comparing these data with data obtained in other laboratories (Schuessler and von Blanckenburg, 2014). Sample analyses were excluded when the drift of isotope ratios between two NBS 28 analyses exceeded ±0.2 ‰ $\delta^{30}Si$ and when they deviated by >0.1 ‰ $\Delta'^{29}Si$ from mass-dependent fractionation trends. Excluding data at this level of precision does not compromise their evaluation for the apparent triple isotope fractionation exponent (θ_{app}). All data failing this criterion fell outside two different mass-dependent relationships, the high-temperature equilibrium isotope fractionations ($\delta'^{29}Si = \delta'^{30}Si \times 0.518$; eq. 15 in Young et al., 2002) and atomic non-equilibrium triple isotope fractionations ($\delta'^{29}Si = \delta'^{30}Si \times 0.509$; eq. 12 in Young et al., 2002). For our external quality control standards measured in the course of this work, we obtained $\delta^{29}Si = -0.13 \pm 0.07$ ‰ and $\delta^{30}Si = -0.26 \pm 0.14$ ‰ (2 s, n = 15) for BHVO-2 and $\delta^{29}Si = -0.70 \pm 0.11$‰ and $\delta^{30}Si = -1.32 \pm 0.18$ ‰ (2 s, n = 7) for IRMM-017. These results are in agreement with previously published values obtained by measurements in solution (Ding et al., 2005; Zambardi and Poitrasson, 2011; Schuessler and von Blanckenburg, 2014; Frick et al., 2016) and by fs laser ablation (Schuessler and von Blanckenburg, 2014; Tatzel et al., 2015; Frick et al., 2016; Steinhoefel et al., 2017). The repeatability of Al/Si in BHVO-2G was 2.3% RSD (n = 15).

3.2. Major element analysis by fs-LA ICP-MS

All major silica phases were additionally analyzed by UV femtosecond laser ablation inductively coupled plasma quadrupole mass spectrometry. Two to three analyses per silica polymorph were done to estimate the total concentration of residual impurities in the silicified carbonate. Due to the gaussian beam shape of the femtosecond laser, small raster was analyzed, similar to the in-situ Silicon isotope analysis. Data were normalized using NIST SRM610 as external standard (Jochum et al., 2011) and the 100 wt% oxide normalization approach (Liu et al., 2008). As quality control standards we analyzed USGS BCR-2 and BIR-1a.

3.3. Oxygen isotope analysis

The triple oxygen isotope composition was analyzed using laser fluorination gas source mass spectrometry. Additionally, high-spatial resolution $\delta^{18}O$ analyses were conducted by secondary ion mass spectrometry (SIMS).

3.4. Laser fluorination

Triple oxygen isotope measurements were carried out by IR laser fluorination method (Sharp, 1990) in combination with a Thermo 253Plus IRMS. Aliquots of approximately 2 mg were loaded into a vacuum chamber and evacuated overnight down to ≈ 3 × 10^{-6} mbar.

The samples were then fluorinated in the presence of 100 mbar of BrF_5 using a 50 W CO_2 laser. Following fluorination, the product gas was purified by employing the same line and protocol as in Pack et al. (2016). The purified O_2 was transferred using a He gas stream (10 mL min^{-1}) to a 5 Å molecular sieve trap located in entrance to the mass spectrometer. After evacuation of He, O_2 was expanded at 50 °C into the bellows of the mass spectrometer and measured in dual inlet mode relative to a reference gas calibrated using O_2 liberated from San Carlos olivine ($\delta^{18}O = 5.23‰$, $\Delta'^{17}O_{0.528} = -52$ ppm; Pack et al., 2016; Sharp et al., 2016; Wostbrock et al., 2020; Pack, 2021). $^{18}O/^{16}O$ and $^{17}O/^{16}O$ ratios are expressed in the δ-notation ($\delta^{17}O$, $\delta^{18}O$) relative to VSMOW. For mass-dependent processes, variations in $\delta^{17}O$ are about half of variations in $\delta^{18}O$. Deviations from such a mass-dependent fractionation line are expressed in form of the $\Delta'^{17}O$ notation (Eq. 1, e.g. Pack, 2021) with:

$$\Delta'^{17}O = 10^3 ln\left(\delta^{17}O + 1\right) - \lambda \bullet 10^3 ln\left(\delta^{18}O + 1\right) \quad (1)$$

where we define the slope λ as 0.528. The analytical repeatability for $\delta^{18}O$ and $\Delta'^{17}O$ are ±0.2 ‰ and ± 6 ppm (1 s), respectively.

3.5. Secondary ion mass spectrometry

Oxygen isotope ratios were determined by SIMS on ca. 200 picogram test portion masses using a Cameca 1280-HR at the GFZ Potsdam. A nominally 10 keV primary $^{133}Cs^+$ beam (2.5 nA, Gaussian shape) with a beam diameter of approx. 8 µm was focused onto the polished sample surface and a 10 * 10 µm raster was used to assure a flat-bottom crater. We used low energy, normal incidence electron flooding for charge compensation during our analyses. Secondary ions were transmitted through the mass spectrometer system that was operated at effectively full transmission using a mass resolution of ΔM/M ≈ 2000 (10% peak height), which is sufficient to resolve ^{18}O from the nearby $^{16}OH_2$ peak. Data acquisition consisted of 20 integrations each lasting 4 s during which our multi-collection system recorded the ^{16}O ion count rate using the L2' Faraday cup (10^{10} Ω resistor) and the ^{18}O on the H2' Faraday cup (10^{11} Ω resistor). Harvard 122,838 quartz sand was used both to correct for instrumental mass fractionation and to assess for time-dependent drift in the $^{18}O/^{16}O$ ratio. We determined the $\delta^{18}O$ value of Harvard 122,838 in a separate analytical session to 22.30 ‰ with a 1 s repeatability of 0.17 ‰ ($n = 160$ determinations). We used this value to calibrate our measurements to NBS 28 which has a published value of $\delta^{18}O_{VSMOW} = 9.579 \pm 0.09$ ‰ (1 s, $n = 8$) (IAEA, 1993; National Institute of Standards and Technology, 2015). For the zero-point on the SMOW δ-scale we use $^{18}O/^{16}O \equiv 0.00200520$ (Baertschi, 1976), and we have directly transferred our measurements to this zero-point. Within the analytical session of the zebra chert, we found a significant dispersion in the $^{18}O^-/^{16}O^-$ data in 'Harvard 122,838' ($n = 32$ analyses on $n = 6$ grains), which lead to repeatabilities of ±0.36 ‰, 1 s). This observation suggests a significant drift in the data and possible problems related at the marginal position of the Harvard reference material. Regarding the absolute δ-values, we consider our results reliable to ±0.36 ‰, which is the best that could be achieved given the drift in isotope ratios in the analytical session.

4. Results

4.1. Silicon isotopes and Al concentrations

Silicon isotope ratios range from −3.56 to 2.11 ‰ $\delta^{30}Si$ ($n = 70$), where 96% of the data ($n = 67$) range from −2.0 to 0.9 ‰ $\delta^{30}Si$. The four silica phases each have distinct Si isotope ratios and show no spatial trend across the section within each polymorph (ca. 2.5 mm), however, they show a systematic decrease with their order of formation as deduced from textural relationships (see section 2.1). Microcrystalline quartz (1) is at 0.41 ± 0.12 ‰ $\delta^{30}Si$ (1 s, $n = 19$) and the lining botryoidal chalcedony (2) at 0.71 ± 0.07 ‰ $\delta^{30}Si$ (1 s, $n = 15$). Fibrous chalcedony is at −1.61 ± 0.22 ‰ (1 s, n = 15) excluding one outlier, with $\delta^{30}Si = -3.56$ ‰. In cryptocrystalline quartz $\delta^{30}Si$ values average − 0.90 ± 0.36 ‰ $\delta^{30}Si$ (1 s, $n = 9$) and represent mostly mixed analyses between the cryptoquartz itself and the intergrown fibrous chalcedony that appears to have penetrated from the contacting fibrous chalcedony veins (4). Comparison of the optically determined modal fraction of chalcedony in the ablation crater (rough estimates of 0, 0.25, 0.5, 0.75) show a strong correlation with measured $\delta^{30}Si$ values and yield an extrapolated end-member composition of −0.65 ‰ for cryptocrystalline quartz (Fig. 3). This value provides an estimate for the lowest $\delta^{30}Si$ of cryptocrystalline quartz. When Al concentrations of the end-member compositions (chalcedony = 129 µg/g; cryptocrystalline quartz = 1027 µg/g; see below) are used to calculate the fraction of chalcedony similar results are obtained (green crosses in Fig. 3). One analysis that contained no visible chalcedony yielded −0.09 ‰ $\delta^{30}Si$ and represents the highest value measured in this phase. The veins of coarse quartz (5) are highly variable with $\delta^{30}Si = 0.39 \pm 0.92$ ‰ (1 s, $n = 11$). The slope in three isotope space (S) of the silica phases microquartz (1), botryoidal chalcedony (2), cryptoquartz (3) and fibrous chalcedony (4) yield an average value of 0.511 ± 0.006 (1 s), not clearly distinguishable between the theoretical θ-value for non-equilibrium stable isotope fractionation of Si isotopes (0.509) and the θ-value for equilibrium fraction (0.518; Young et al., 2002).

Average Al concentrations (all 1 s) are 654 ± 91 µg/g in microcrystalline quartz (1) and 703 ± 77 µg/g in botryoidal chalcedony (2). Cryptocrystalline quartz (3) mixed with fibrous chalcedony (4) averages 484 ± 245 µg/g, where pure cryptocrystalline quartz shows the highest value measured of 1027 µg/g. Low Al concentrations are found in chalcedony (4) with 129 ± 96 µg/g. Three analyses of chalcedony in the cryptocrystalline quartz domain have elevated Al concentrations of between 299 and 324 µg/g. Excluding these data the average concentration is at 86 ± 25 µg/g. Vein quartz contains 103 ± 68 µg/g Al.

4.2. Chemical composition (fs LA ICP-MS)

Al concentrations determined by MC-ICP-MS were verified by quadrupole fs LA ICP-MS analyses. All silica phases analyzed for major and trace elements (microcrystalline quartz (1), cryptocrystalline quartz (3) and chalcedony (4)) are very pure and contain <4300 µg/g Na, < 1000 µg/g Al, < 2000 µg/g K, < 2700 µg/g Fe and < 1100 µg/g Zn. Chalcedony veins contain the least amount of impurities, mostly lower than their detection limits. Microcrystalline quartz (1) and cryptocrystalline quartz (3) contain ca. 600–1000 µg/g Al, 700–1300 µg/g K and 500–1100 µg/g Zn and very spotty Fe (Table 1).

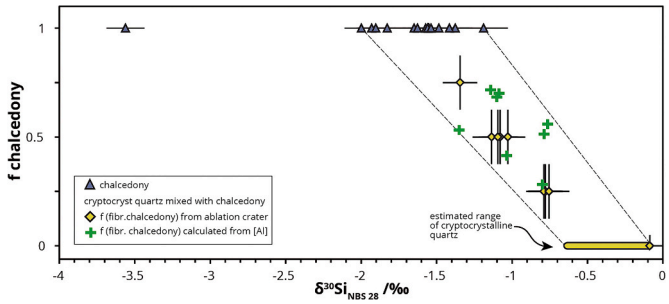

Fig. 3. Measured $\delta^{30}Si$ values in fibrous chalcedony and cryptocrystalline quartz with optically estimated proportions of the fibrous chalcedony in analyses of cryptocrystalline quartz (cf. Fig. 1e). The estimated range of $\delta^{30}Si$ values in cryptocrystalline quartz (yellow band) is spanned by the extrapolated mixing trend and one data point in pure cryptocrystalline quartz. (For interpretation of the references to colour in this figure legend, the reader is referred to the web version of this article.)

Table 1
Concentrations (μg/g) of selected elements analyzed by fs LA-ICP-MS. LODs are based on estimation of the background signal and NIST610, following the procedure outlined in Longerich et al. (1996). Calcium was below the limits of detection (1300 μg/g) in all samples.

	Si	Al	Na	Fe	Zn
Microcrystalline quartz (1)	464,300	578	2110	<LOD (10)	558
Microcrystalline quartz (1)	456,924	1003	4256	2669	1062
Cryptocrystalline quartz (3)	464,987	873	886	<LOD (10)	509
Cryptocrystalline quartz (3)	462,160	907	1786	2489	700
Chalcedony (4)	466,888	<LOD (20)	561	<LOD (10)	<LOD (18)
Chalcedony (4)	466,947	<LOD (20)	746	<LOD (10)	<LOD (18)
Chalcedony (4)	466,210	<LOD (20)	1327	<LOD (10)	443
mixed analysis of (1) and (2)	466,834	<LOD 738	<LOD (166)	<LOD (10)	<LOD (18)
mixed analysis of (2) and (4)	465,924	752	426	<LOD (10)	477

4.3. Oxygen isotopes

Laser fluorination analyses yield $\delta^{18}O$ values in overall agreement with SIMS data (Table 2, Fig. 5). Oxygen isotope ratios range from 23.80 to 29.02 ‰ $\delta^{18}O_{VSMOW}$ on the microscale ($n = 233$). Microcrystalline quartz (1) averages 27.05 ‰ ± 0.45 (1 s, $n = 50$), botryoidal chalcedony (2) 26.47 ‰ ± 0.46 (1 s, n = 50), cryptocrystalline quartz (3) 26.16 ‰ ± 0.27 (1 s, $n = 67$), chalcedony (4) 26.10 ‰ ± 0.53 (1 s, $n = 32$), vein quartz (5) 25.53 ‰ ± 1.45 (1 s, $n = 37$). The small deviations from the bulk data result from difficulties of spatially precise sampling by drilling.

$\Delta'^{17}O$ values of microquartz (1), and cryptocrystalline quartz (3), chalcedony (4) are identical within the analytical repeaetability of 6 ppm and average − 89 ppm relative to the equilibrium line with $\lambda = 0.528$. Cross-cutting vein quartz (5) has a distinct $\Delta'^{17}O$ value of −70 ppm.

A transect across the quartz vein (5) reveals a zonation in $\delta^{18}O$ that encompasses a range of 4–5 ‰ (Fig. 6 a). $\delta^{18}O$ is highest at the walls and increases steeply towards the center of the ca. 1 mm wide vein. A second transect through the vein, where its diameter amounts only ca. 0.6 mm shows this trend only in a very diminished form. The surrounding silica phases have a reduced $\delta^{18}O$ within approx. 50 μm distance to the vein contact.

5. Discussion

5.1. Decreasing $\delta^{18}O$ during replacement

While the microscale $\delta^{18}O$ values scatter considerably by ca. 2 ‰ within each type of silica and overlap with one another, there is an apparent decrease of average $\delta^{18}O$ values with successive silica formation (Fig. 5), excluding the coarse quartz (5) (see below). A decrease in $\delta^{18}O$ is the expected sign of change for fractionation in a finite reservoir ($\varepsilon^{18}O > 0$). However, reservoir effects are basically absent through the high abundance of oxygen in water where precipitation will yield no measurable change in $\delta^{18}O$: For example, a solution saturated with respect to opal-A at 60 °C containing 216 μg/mL dissolved SiO_2 (Gunnarsson and Arnórsson, 2000) can remove only ca. 0.01% of the oxygen from solution when silica is precipitated until the saturation with respect to quartz (27 μg/mL) is achieved. In a closed system, it appears unlikely that the fluids' $\delta^{18}O$ could have decreased by ca. 1–2 ‰ over the course of silicification. Instead, the decrease in $\delta^{18}O$ could reflect increasing diagenetic temperatures during successive silicification. Using the temperature calibration of Sharp et al. (2016), the decrease of average $\delta^{18}O$ values corresponds to an increase in temperatures of 4–7 °C when the fluid is assumed to be constant in the range of −5 to +5 ‰ $\delta^{18}O$. This relatively low temperature range is likely responsible for the overlap in $\delta^{18}O$ values of the successively formed silica phases. Their scatter in $\delta^{18}O$ reflects both, the limited of analytical precision of 0.36 ‰ (1 s; see section 3.3) as well as the natural variability within the sample.

The steeply increasing $\delta^{18}O$ towards the center of the veins likely reflects cooling with ongoing quartz precipitation in the vein. This $\delta^{18}O$ difference corresponds to a temperature difference of ca. 20–35 °C for fluid compositions between −5 to +5 ‰ $\delta^{18}O$. The trend in the thinner vein (Fig. 6b) might not be as developed because precipitation ended earlier than in the ticker vein and thus records only a limited cooling trend. The lowered $\delta^{18}O$ values in the immediate contact zone suggest that alteration of the original $\delta^{18}O$ signature reached only over short distances of <50 μm.

5.2. Decreasing $\delta^{30}Si$ during replacement

The large $\delta^{30}Si$ range at the μm to mm scale in silicified zebra dolomite can be explained by (i) changes in $\delta^{30}Si_{fluid}$, (ii) differences in isotope fractionation during replacement of the different precursor carbonate crystals and during precipitation of silica into void space, and (iii) by reservoir effects or by any combination of these effects. In the following we discuss the feasibility of these scenarios- also given the systematic variations in $\delta^{18}O$ and elaborate on the testable case (iii).

5.2.1. A changing $\delta^{30}Si$ composition of the silicifying fluids over the course of silicification

Two major silica sources are indicated in the study site. Petrographic evidence shows that siliceous sponge spicules were present in this coastal shallow marine environment (Tatzel et al., 2020). A large variation in $\delta^{30}Si$ of the silica sources is indicated by the presence of sponge spicules that fractionate Si isotopes by up to 6 ‰ at high dissolved silicon (dSi) concentrations (Wille et al., 2010; Hendry and Robinson, 2012). DSi concentrations might have been as high as 1 mM in the Precambrian and Early Cambrian (Siever, 1992; Racki and Cordey, 2000) and would have allowed for inorganic silica precipitation from seawater as well. As $\varepsilon^{30/28}Si_{silica/fluid}$ can be near-zero (Oelze et al., 2015; Tatzel et al., 2015), a maximum theoretical range of 6 ‰ $\delta^{30}Si$ in silica sources is possible. Assuming seawater $\delta^{30}Si = 2$ ‰ (Robert and Chaussidon, 2006; Marin-Carbonne et al., 2014), sponge spicules could have been as low as −4 ‰ $\delta^{30}Si$. This large range suggests that a change in silicon sources during silicification can principally explain the range of observed $\delta^{30}Si$-values.

Table 2
Oxygen isotope data of various silica phases analyzed by laser fluorination and SIMS.

	Bulk $\delta^{18}O_{VSMOW}$ /‰	Bulk $\delta^{17}O_{VSMOW}$ /‰	$\Delta'^{17}O_{0.528}$	SIMS $\delta^{18}O_{VSMOW}$ /‰	1 s	n
Microquartz (1)	26.22	13.668	−0.089	27.05	0.45	50
Botryoidal chalcedony (2)	n.m.	n.m.	n.m.	26.47	0.46	50
Cryptocrystalline quartz (3)	26.63	13.69	−0.092	26.16	0.27	67
Chalcedony (4)	24.88	12.972	−0.085	26.10	0.53	32
Vein quartz (5)	24.78	12.939	−0.070	25.53	1.45	37

Such selectivity of silica dissolution from siliceous sediments is documented in $\delta^{30}Si$ of early diagenetically formed porcellanite (Tatzel et al., 2015). Early diagenetic dissolution of labile silica leads to Si saturation of pore waters, effectively stopping further silica dissolution (Van Cappellen and Qiu, 1997a, 1997b). Hence, this explanation requires multiple steps of dissolution-oversaturation-precipitation and a simultaneous change in fluid $\delta^{30}Si$ by ca. 2.4 ‰. While this scenario is plausible it cannot be further tested.

5.2.2. *Variations in $\varepsilon^{30/28}Si_{silica/fluid}$ during silica-for-carbonate replacement and precipitation of silica*

The differences in $\delta^{30}Si$ in zebra chert can be explained by differences in $\varepsilon^{30/28}Si_{silica/fluid}$ of up to ca. 2.4 ‰, assuming that the $\delta^{30}Si$ of the fluid remained constant. Differences of up to 3 ‰ $\delta^{30}Si$ can be obtained just by changing the net rates of silica precipitation (Geilert et al., 2014a; Oelze et al., 2014; Oelze et al., 2015). The underlying reason for rate variations can be differences in the degree of silica supersaturation. High degrees of supersaturation lead to high net precipitation rates that are associated with a stronger kinetic isotope fractionation with preference for ^{28}Si. As the crystal size is expected to decrease with increasing net silica precipitation rates (Folk and Pittman, 1971), smaller quartz crystals ought to be enriched in ^{28}Si compared to larger crystals - if kinetics were the controlling factor. However, the opposite is observed, arguing against precipitation rate as controlling factor on $\delta^{30}Si$ during silicification.

Chemical factors might also play a role in determining the silica transformation rates during silica diagenesis, such as preferential silicification in the presence of organic matter (Hinman, 1990; Andrade et al., 2020), by salt concentrations (Marshall and Warakomski, 1980), or by other cations that modify the silica solubility (Hinman, 1998). If this is also true for silica replacement, composition-dependence of $\delta^{30}Si$ values would have to be observed. Different silica phases indeed show distinct $\delta^{30}Si$ values and Al concentrations (Fig. 4). All silica phases with Al concentrations >400 µg/g (microcrystalline quartz (1), botryoidal chalcedony (2) and cryptocrystalline quartz (3)) have $\delta^{30}Si$ values > -0.6 ‰. Fibrous chalcedony has lower Al concentrations and $\delta^{30}Si < -1.19$ ‰. This could suggest that the presence of Al-bearing components influences Si isotope fractionation during silica-for-carbonate replacement. The influence of Al on Si isotope fractionation was previously shown experimentally (Oelze et al., 2015) and could suggest that silica polymerization is supported by the presence of Al and allow for near quantitative precipitation, causing $\delta^{30}Si_{precipitate} \approx \delta^{30}Si_{fluid}$. Conversely, in the absence of Al, higher degrees of supersaturation upon silica precipitation are possible, thus causing far-from equilibrium conditions. These result in a kinetic isotope fractionation effect that leads to a more negative $\delta^{30}Si$. We note that microcrystalline quartz and botryoidal chalcedony each have narrow and distinct ranges of $\delta^{30}Si$ values but similar ranges of Al concentrations from ca. 430 to 830 µg/g. This doubling in Al concentrations at constant $\delta^{30}Si$ in both phases suggests that no dependence on the substrates' Al concentration exist – at least in this relatively low concentration range.

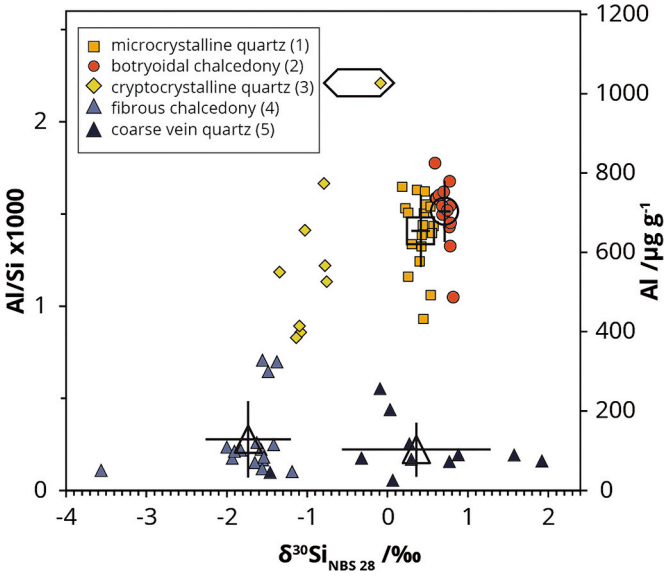

Fig. 4. $\delta^{30}Si$ values versus Al/Si ratios in the silicified zebra dolomite. Each silica phase plots in a distinctive region with almost no overlap to the other phases. Average values (with 1 s) are shown by larger, open symbols. The large $\delta^{30}Si$ range of cryptocrystalline quartz (3) is caused by mixed analyses with the intergrown fibrous chalcedony (cf. Fig. 3).

5.2.3. *Reservoir effects control Si isotope fractionation*

When a system that contains a fixed amount of an element that is nearly quantitatively transferred from the educt phase (e.g. a solution) to the product phase (e.g. a solid), large isotopic variations can develop on the sub-system scale. The resulting range in isotope ratios depends on 1) the isotope fractionation factor(s), 2) if educt and product remain in exchange ('closed-system equilibrium') or if they are isolated from one another ('Rayleigh distillation' or 'open system' fractionation), and 3) the spatial analytical resolution. Notably, Rayleigh distillation does not imply that isotope fractionation must occur under non-equilibrium ('kinetic') conditions. For slow reactions, the instantaneous product and educt can remain in equilibrium before the isolation of the product phase from the system, thus allowing for the establishment of an isotopic equilibrium in a finite system described by Rayleigh distillation equations (Johnson et al., 2004). With other words, silica would be isotopically fractionated in equilibrium with no back-reaction with the remaining solution; quantitative precipitation would then lead to an isotopic evolution following Rayleigh-fractionation laws, but not with a kinetic isotope fractionation effect. Hence, Rayleigh-behavior and equilibrium isotope effects are no contradiction. Previously observed large $\delta^{30}Si$ variations in authigenic quartz and silicified carbonate have also been explained by Rayleigh distillation in a finite reservoir (Chen et al., 2016; Andrade et al., 2020). Their work suggests that lower mass Si isotopes are preferentially incorporated into solids as is widely observed for silica precipitation and adsorption at low temperature (Delstanche et al., 2009; Geilert et al., 2014a; Oelze et al., 2014; Oelze et al., 2015; Chen et al., 2016; Ding et al., 2017).

5.3. *Equilibrium open-system model*

To explore reservoir effects as cause of the isotopic variation, we use constraints on the order of precipitation (see section 2.1), the progress of the reaction (amount of Si precipitated, f_{prec}), and the fluid's $\delta^{30}Si$. In the following we derive these constraints to assess Si isotope fractionation during silicification. First, we derive the order of precipitation from textural relationships (Fig. 1). We note that overgrowths of botryoidal chalcedony (2) can form early diagenetically on carbonates (e.g. Papineau et al., 2021), suggesting it could have formed first. Regardless, the general order of formation clearly shows that silica phases with high $\delta^{30}Si$ must have formed prior to those with lower $\delta^{30}Si$. This suggests $\varepsilon^{30/28}Si > 0$, as has recently been shown for experimentally precipitated quartz (Pollington et al., 2016) and in a sinter where ^{30}Si-enriched quartz ($\Delta^{30/28}Si = 1.1$ to 2.8 ‰) formed by precipitation from a 50 to 75 °C warm fluid (Wang et al., 2021). These observations are in line with ab initio models that predict the preferential and temperature-dependent ^{30}Si incorporation into quartz ($\varepsilon^{30/28}Si_{quartz/H4SiO4} > 0$) at chemical equilibrium (Dupuis et al., 2015).

The presence of a hot, Si-rich fluid phase is not supported by geological, petrographical or isotopic evidence. Rather the dissolution of amorphous silica during burial would let pore waters attain saturation with respect to amorphous silica at diagenetic temperatures. Silica precipitation would have ended when ongoing silica precipitation decreased dSi concentrations to the equilibrium solubility of quartz or

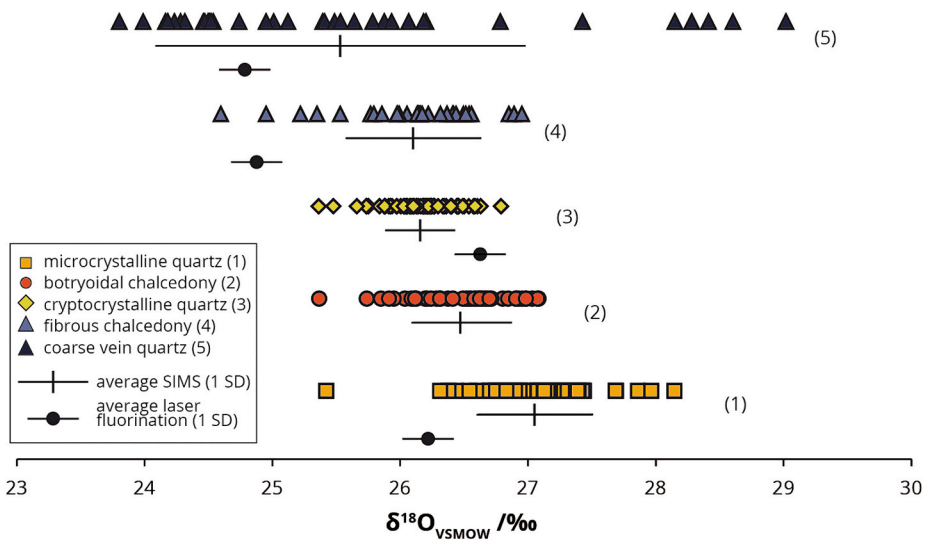

Fig. 5. Oxygen isotope ratios in the silicified zebra dolomite. The numbers correspond to the order of precipitation as suggested by textural relationships (cf. Fig. 1). Average $\delta^{18}O$ values are successively lower along the sequence of silica replacement. The bulk $\delta^{18}O$ values can be offset from the average $\delta^{18}O$ values measured by SIMS due to the chance of unwanted sampling of neighboring phases by drilling.

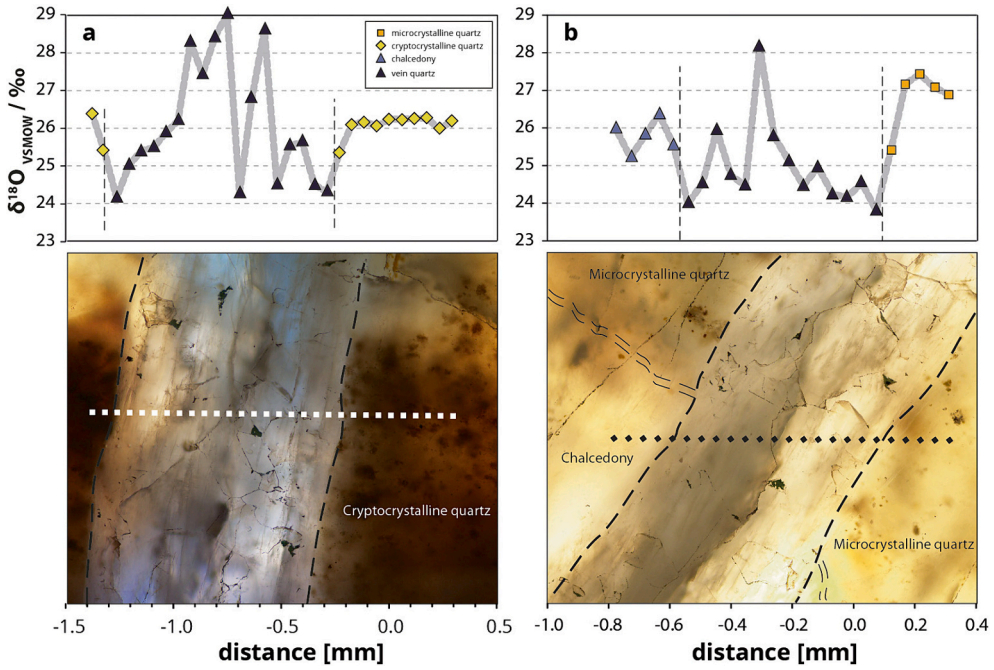

Fig. 6. Transmitted light images (epoxy-mounted thick section) of SIMS $\delta^{18}O$ transects across the cross-cutting quartz vein (5). The walls of the vein yield the lowest $\delta^{18}O$ values and increase towards the center. $\delta^{18}O$ values of surrounding silica is reduced at the contact to the vein.

chalcedony. The relative amount of Si that can be precipitated ($f_{prec\ max}$) is thus given by the ratio of the solubility products K_{SP} of opal-A and quartz, termed 'solubility ratio' (Chen et al., 2016, 2020) – a ratio that changes with temperature. We thus estimate $f_{prec\ max}$ from a first rough estimate of diagenetic temperatures of quartz formation from $\delta^{18}O_{chert}$ assuming $\delta^{18}O_{fluid} = 0$ to -2 ‰. The choice of $\delta^{18}O_{fluid}$ has no strong leverage on the calculated maximum relative amount of Si precipitation as we demonstrate below. Using the calibration of Sharp et al. (2016) – that is well defined in the low to medium temperature range compared to other calibrations – temperatures of 60 to 70 °C are obtained. The ratio of solubility products K_{SP}(opal-A) to K_{SP}(quartz) amounts to 0.87 to 0.88 when the equilibrium constants from Gunnarsson and Arnórsson (2000) are used. This also puts constraints on the starting composition of the $\delta^{30}Si$ of the fluid: upon 87 to 88% precipitation the cumulative $\delta^{30}Si$ must equal the $\delta^{30}Si$ bulk sample.

We also assume that the modal abundances of all subsequently replaced carbonate phases in our sample sum up to yield to total of the sample, recording the full replacement history. This assumption is justified by the presence of various silica phases that form a relatively continuous array of $\delta^{30}Si$-values. It follows that the volume fractions of the silica phase correspond to the reaction progress quantified by f_{prec}. The volume fractions of all silica phases are thus derived from relative modal abundances in the thin section and amount to ca. 1% botryoidal chalcedony, 42% microcrystalline quartz, 28% cryptocrystalline quartz and 28% fibrous chalcedony when the later formed, cross-cutting vein of coarse quartz is omitted. Consequently, in a Rayleigh distillation model

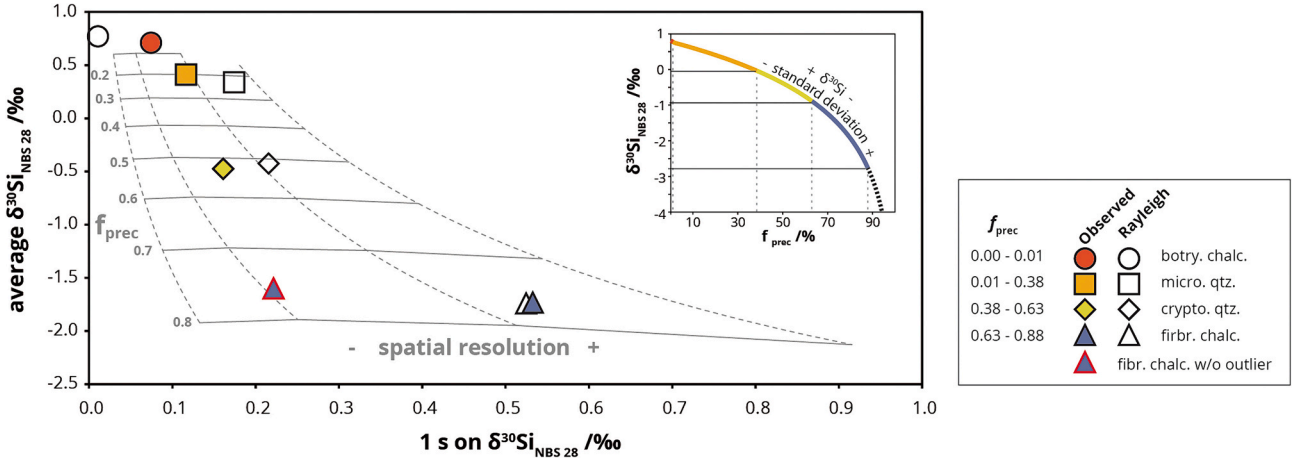

Fig. 7. Relationship between average δ^{30}Si and standard deviation of silica phases (colored symbols) compared to the δ^{30}Si-s relationship in instantaneous precipitates of a Rayleigh model (open symbols). The calculated δ^{30}Si-s relationship is based on δ^{30}Si(fluid) = −0.9 ‰ and $\varepsilon^{30/28}$Si = 1.68 ‰ (see main text). The increase in s and simultaneous decrease of average δ^{30}Si values along the sequence of precipitation supports the finite-reservoir assumption and thus the positive $\varepsilon^{30/28}$Si. The standard deviation increases with increasing spatial resolution. The s of cryptocrystalline quartz is based on δ^{30}Si values corrected for the unavoidable contribution of fibrous chalcedony during analysis. For this calculation the fibrous chalcedony endmember is assumed to have δ^{30}Si = −1.61 ‰ (this average value excludes the outlier at −3.56 ‰; cf. Fig. 3). The high s of fibrous chalcedony (0.53 ‰) is owed to this (analytically sound) outlier. When it is excluded, s reduces to 0.22 ‰ (red rim; cf. Fig. 4). (For interpretation of the references to colour in this figure legend, the reader is referred to the web version of this article.)

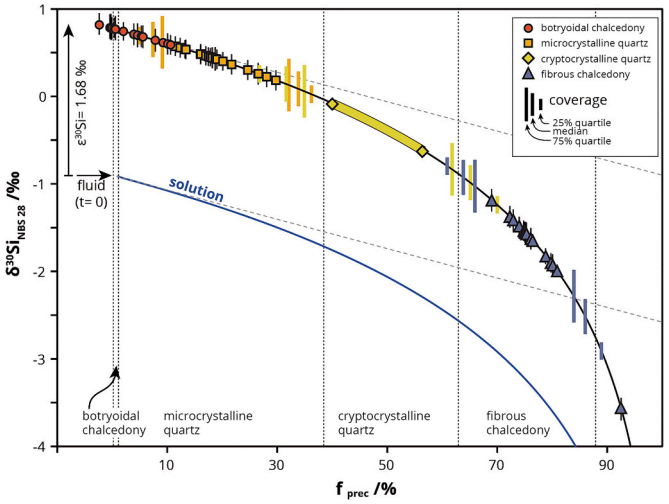

Fig. 8. Rayleigh model for the silicified zebra dolomite. The x-axis shows the progressing silicification (f_{prec}), where the modal abundances of all silica phases (vertical dotted lines) sum up to ca. 88% (= $f_{prec\ max}$ = ratio of solubilities of opal-A to quartz at formation temperature; see main text). The δ^{30}Si values are sorted in descending order and each has a calculated f_{prec} value that depends on the $\varepsilon^{30/28}$Si value and fluids' δ^{30}Si starting composition (−0.9 ‰; constrained by the cumulative δ^{30}Si at $f_{prec\ max}$ = $\delta^{30}Si_{bulk}$; see main text). The statistical chance of incomplete sampling the f_{prec} ranges is accounted for by extended data ranges that are shown by colored vertical bars that represent the 25%, 50% and 75% quartiles. The measured data fit best into the f_{prec} ranges when $\varepsilon^{30/28}$Si = 1.68 ‰, but also fit between $\varepsilon^{30/28}$Si = 1.5 ‰ and 1.8‰, supporting fractionation of a finite Si reservoir with no back-reaction of product and educt. Botryoidal chalcedony is assumed to have formed before microcrystalline quartz. Its wide f_{prec} range compared to its modal abundance of ca. 1.3% is presumably an artifact that stems from its δ^{30}Si range being likely smaller than the analytical precision (see section 5.3). If botryoidal chalcedony formed after microcrystalline quartz, it must be associated with a lower $\varepsilon^{30/28}$Si.

the cumulative modal abundances of subsequently formed silica phases serve as 'calibration points' where each phase represents a f_{prec}-range delimited by two such markers of the reaction progress.

The measured δ^{30}Si values of the subsequent silica phases therefore represent the temporal evolution (f_{prec}) of the fluid offset by $\varepsilon^{30/28}$Si. For each measured δ^{30}Si-value a corresponding f_{prec} value can be calculated that depends on the δ^{30}Si starting composition of the fluid (fixed by $\delta^{30}Si_{bulk}$ and $f_{prec\ max}$) and $\varepsilon^{30/28}$Si. It follows that in this system the best fit $\varepsilon^{30/28}$Si can be solved when all system requirements are met.

5.3.1. *Statistical coverage and spatial resolution*

Before we proceed with this analysis, we evaluate the completeness of sampling of the f_{prec} range, i.e. the 'instantaneous curve' with the spatial resolution of our laser ablation method. This assessment is important, as it has bearings on the actual f_{prec} range of each quartz phase analyzed and hence also on the permissible $\varepsilon^{30/28}$Si range. Two factors need to be considered, the analytical spatial resolution and precision and the statistical coverage.

To evaluate the spatial resolution of instantaneous precipitates and further scrutinize the assumption of isotope fractionation in a finite Si reservoir, we exploit the characteristic relationship between average δ^{30}Si and the standard deviation (s) within f_{prec} ranges of each silica polymorph, i.e. the part of the reaction progress they represent. In Rayleigh distillation, there is an inherent increase in the rate of change of δ^{30}Si of subsequent instantaneous precipitates with ongoing reaction progress, i.e. the 'instantaneous curve' steepens with ongoing precipitation f_{prec}. This means that the standard deviation increases for a given f_{prec} range towards higher f_{prec}, because the δ^{30}Si-range increases with reaction progress (cf. inset in Fig. 7). The spatial resolution – the volume analyzed by laser ablation relative to the crystal size – thereby determines how well the instantaneous precipitates can be resolved. The standard deviation within each silica polymorph's data population thus increases during subsequent precipitation in a magnitude depending on the spatial resolution. For an infinite spatial resolution, one could fully sample the instantaneous precipitates that populate the Rayleigh curve. Any lower spatial resolution will integrate the δ^{30}Si values, resulting in a lower range of values, thus decreasing the standard deviation. Fig. 7 shows the predicted increase in standard deviation and decrease in average δ^{30}Si with reaction progress. We compare measured δ^{30}Si -s relationships for all silica phases with δ^{30}Si -s relationships in a Rayleigh distillation for the same f_{prec} ranges. We observe an increase in the standard deviation with subsequent silica precipitation. Notably, botryoidal chalcedony represents only ca. 1.3% of the total Si, and therefore its actual δ^{30}Si-range is likely lower than the analytical precision (2 SE) of ca. 0.10–0.16 ‰ δ^{30}Si allows resolving. This leads to the artifact of a widened f_{prec} range in a Rayleigh model. This effect is

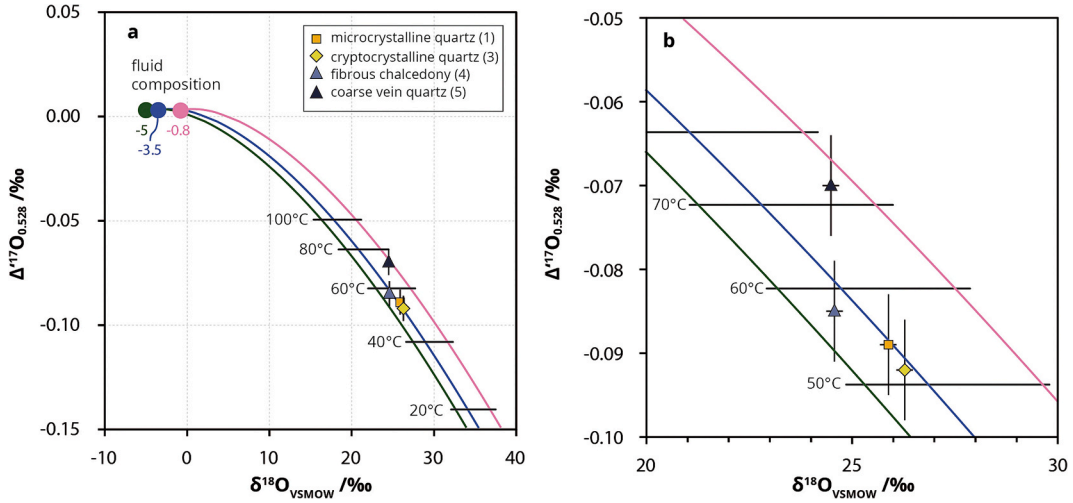

Fig. 9. Triple oxygen isotope composition of silica phases in the silicified zebra dolostone. Microcrystalline quartz, cryptocrystalline quartz and fibrous chalcedony plot within 0.002 ‰ on the equilibrium line originating in $\delta^{18}O_{fluid} = -3.5$ ‰ and $\Delta'^{17}O = 0.003$ ‰ (blue line). The green and pink lines show the equilibrium isotope fractionation trend for $\delta^{18}O_{fluid} = -5$ ‰ and − 0.8 ‰ (silicification temperatures of 45 °C and 65 °C, respectively; see main text). b is a magnification of the data in a. (For interpretation of the references to colour in this figure legend, the reader is referred to the web version of this article.)

especially strong for early formed solids (low f_{prec}), because the instantaneous curve has a shallow slope at low f_{prec} and a small increase in the range of $\delta^{30}Si$ thus translates to a comparatively large range of f_{prec}.

There is a statistical chance that our analyses do not represent the true full $\delta^{30}Si$ range. We assess the statistical coverage of $\delta^{30}Si$ values in each f_{prec} range using a Monte Carlo sampling approach. For this assessment we assume that the Rayleigh curve is resolved on the percent-level, i.e. the changes in $\delta^{30}Si$ can be resolved analytically in 1% increments of the instantaneous curve. Within each pair of calibration points (f_{prec} –ranges that represent one of the four silica phases; see above) – we randomly select n values corresponding to the number of isotope analyses per silica polymorph. Their range relative to the full $\delta^{30}Si$ range of values within the respective f_{prec} range corresponds to the completeness of sampling of the respective f_{prec} range. We refer to this as the 'coverage factor' (full coverage: $f_c = 1$). The statistical coverage (median values) of our analyses are f_c(microcrystalline quartz) = 0.92, f_c(botryoidal chalcedony) = 0.89, f_c(cryptocrystalline quartz) = 0.83, and f_c(fibrous chalcedony) = 0.90. This means that statistically, 8 to 17% of the data populations in the respective f_{prec} ranges are missing. To account for the statistical chance of missing lower and higher values in each phase, we also show an extension to the range of measured $\delta^{30}Si$ values (Fig. 8; vertical bars) by 1- f_c equally distributed to the lower and high end of the measured range. We plot the 25% confidence interval, the median, and the 75% confidence intervals of 1-f_c (Fig. 8). While the exact resolution of the f_{prec}-range remains unknown, the Monte Carlo approach suggests a high coverage. We also conclude that the spatial resolution must be relatively high, because the 'gaps' in population between two adjacent silica phases are relatively small.

We thus proceed to fit the $\delta^{30}Si$ values of all silica types into the respective f_{prec} ranges while meeting the boundary conditions (last precipitation at $f_{prec\ max}$ and $\delta^{30}Si_{bulk}$ = cumulative $\delta^{30}Si$ at $f_{prec\ max}$) by adjusting $\varepsilon^{30/28}Si_{quartz/H4SiO4}$. There is some uncertainty on the f_{prec} ranges due to the fact that modal abundances are deduced from a 2-D section throughout the rock. Secondly, uncertainties in temperature estimates (stemming from uncertainties in the $\delta^{18}O_{fluid}$) would only have a minimal impact on the f_{prec} ranges and hence also play no significant role in fitting (the strongly temperature-dependent) $\varepsilon^{30/28}Si_{quartz/H4SiO4}$ (see section 5.4). Relative temperature differences between the different silica phases are minimal (4–7 °C; see section 5.1) and hence do not change $\varepsilon^{30/28}Si$ significantly either.

The fluid $\delta^{30}Si$ is no variable in the open-system model, because the cumulative $\delta^{30}Si$ at $f_{prec\ max}$ (derived from the solubility ratio, see section 5.3) must equal $\delta^{30}Si_{bulk}$. Here, upon ca. 88% silica precipitation ($f_{prec\ max}$) the cumulative $\delta^{30}Si$ must equal −0.42 ‰, the bulk rock value determined as the average $\delta^{30}Si$ values of each silica polymorph weighed with their modal abundances. Only a range of coupled values for $\delta^{30}Si_{fluid}$ and $\varepsilon^{30/28}Si$ fulfill the requirement of cumulative $\delta^{30}Si$ (instantaneous curve) to equal −0.42 ‰. We determine the best fit $\varepsilon^{30/28}Si$ by minimizing the differences between measured and calculated average $\delta^{30}Si$ for all f_{prec} ranges. The best fit is obtained when $\varepsilon^{30/28}Si$ = 1.68 ‰. In the model we assume that botryoidal chalcedony formed first onto a not yet silicified carbonate layer (see section 2.1). We note that if it formed after microcrystalline quartz, it must be associated with a lower $\varepsilon^{30/28}Si$, because then it would have formed at a higher f_{prec}. Due to its low overall volume of ca. 1.3%, the botryoidal chalcedony does not compromise the approach to assess $\varepsilon^{30/28}Si$. For this choice of $\varepsilon^{30/28}Si$, $\delta^{30}Si_{fluid}$ equals −0.9 ‰.

5.4. Si isotope thermometry

We use the estimated $\varepsilon^{30/28}Si$ and the T- $\varepsilon^{30/28}Si$ dependence for Si precipitation at chemical equilibrium (Dupuis et al., 2015) to assess the temperatures of silicification independently of $\delta^{18}O$. This requires that a chemical equilibrium existed during the slow precipitation with an effective isolation from the system. We discount pH-speciation effects on $\delta^{30}Si$ that result from the strong fractionation between H_4SiO_4 and $H_3SiO_4^-$ with $\varepsilon^{30/28}Si_{H3SiO4\text{-}H4SiO4}$ between approx. -2.3 and − 2.2‰ at T = 25 °C and T = 75 °C, respectively (Stamm et al., 2019). In the case of silicified carbonates, it can be assumed that the pH was buffered at near-neutral conditions, thus suggesting the vast predominance of H_4SiO_4.

At equilibrium, the magnitude of Si isotope fractionation between quartz and H_4SiO_4 depends on temperature where the T-dependence is described by $1000 \ln\alpha = -4.7\ (100/T)^2 - 42.3\ (100/T)^3$ (T in K; Dupuis et al., 2015). Therefore, when the isotopic fractionation (ε) is known, temperatures can be derived. The best fit is achieved at $\varepsilon^{30/28}Si$ is 1.68‰, corresponding to 52 °C, but we note that the measured $\delta^{30}Si$ values fall into the respective f_{prec} ranges for $\varepsilon^{30/28}Si$ = 1.5 to 1.8‰, translating to silicification temperatures in the broader range of 45 to 65 °C. If these temperature ranges are taken at face value, the fluid $\delta^{18}O$ must have been between approx. -5‰ (45 °C) and − 0.8‰ (65 °C) to reconcile $\delta^{18}O_{chert}$. Accordingly, both O-isotope thermometry and the presented approach using Si isotopes yield the same temperatures when the fluid was slightly depleted in ^{18}O: for the best fit $\varepsilon^{30/28}Si$ of 1.68 ‰,

$\delta^{18}O_{fluid}$ must be −3.5‰. The temperatures of silicification are thus lower than O isotope thermometry would suggest in the absence of constraints of $\delta^{18}O_{fluid}$ (and assuming $\delta^{18}O_{fluid} = 0$). This somewhat lower temperature estimate fixes the solubility ratio (see section 5.2) at the higher end of estimates (0.88) with no significant effect on the f_{prec} ranges.

The required equilibrium conditions for temperature-dependent Si isotope fractionation could not be demonstrated from the triple Si isotope composition due to an insufficient analytical precision. The triple oxygen isotope composition plots somewhat below the equilibrium line when the fluid is assumed to have had $\delta^{18}O = 0‰$ and $\Delta'^{17}O = 0‰$. In fact, the majority of Precambrian cherts are found to plot below the equilibrium line originating in the modern seawater oxygen isotope composition, a phenomenon explained by meteoric alteration or hydrothermal silica precipitation in the Archean (Sengupta et al., 2020; Wostbrock and Sharp, 2021; Zakharov et al., 2021). However, when the $\delta^{18}O_{fluid}$ is at ca. -3.5 ‰ as our analysis based on Si isotope data suggests and $\Delta'^{17}O = 0.003‰$ -as estimate for seawater at the time (Guo et al., 2022), microcrystalline quartz, cryptocrystalline quartz and fibrous chalcedony fall within 0.002 ‰ onto the triple O-isotope equilibrium line (Fig. 9). Vein quartz plots minimally (0.013 ‰) above the equilibrium line.

The isolated system with a finite Si reservoir can be reconciled geologically by the simple consideration that the recorded temperatures of approx. 50 °C suggest that silicification occurred when the sediment was buried to at least one kilometer depth, but likely more. Silica transformation kinetics suggest that the overlying siliceous sediments had already transformed to chert when the carbonate was silicified (Tatzel et al., 2022). Thus, the cherts would have served as impermeable layer that impeded further input of (isotopically unfractionated) Si. The replacement of zebra dolomite by silica was presumably driven by the CO_2-release from the decomposition of organic matter enclosed in carbonate. The presence of botryoidal chalcedony might testify to the role of organic matter decomposition (Papineau et al., 2021).

6. Conclusions

In the absence of evidence for differences in $\varepsilon^{30/28}Si$ for different silica polymorphs and possible changes in the fluid $\delta^{30}Si$ during silicification, we suggest that the currently best explanation for the decreasing $\delta^{18}O$ and $\delta^{30}Si$ during subsequent silica-for-carbonate replacement is Si isotope fractionation in chemical equilibrium associated with positive $\varepsilon^{30/28}Si$ in a finite Si reservoir during burial diagenesis at temperatures of approx. 50 °C. To reconcile $\delta^{30}Si$-derived temperatures of silicification with $\delta^{18}O$ the fluid must have been between −2.5 to −4 ‰ $\delta^{18}O$. These inferred $\delta^{18}O_{fluid}$ values coincide with the seawater $\delta^{18}O$ composition predicted for the Late Precambrian by a recent seawater $\delta^{18}O$ evolution model (Guo et al., 2022). For this $\delta^{18}O_{fluid}$ range, the silicified dolostone falls onto the triple oxygen isotope equilibrium curve. This contrasts with most Precambrian cherts that fall below the equilibrium line. ^{17}O-depletion is observed already in amorphous silica precursors that transform diagenetically to chert (Ibarra et al., 2022). The lack of such ^{17}O-depletion could hint at direct quartz precipitation or the absence of other authigenic phases competing with silica for ^{18}O. Should silicification generally occur in Si isotopic equilibrium, temperatures of silicification can be derived from Si isotopes and the fluid $\delta^{18}O$ can be constrained, allowing the reconstruction of the seawater $\delta^{18}O$ composition and temperature in deep geological time. Temperature-dependent Si-isotope fractionation with $\varepsilon^{30/28}Si > 0$ could thus also provide an alternative explanation for ^{30}Si-rich, silicified rocks of the Precambrian.

CRediT authorship contribution statement

Michael Tatzel: Writing – review & editing, Writing – original draft, Supervision, Investigation, Formal analysis, Conceptualization. **Marcus Oelze:** Writing – review & editing, Investigation, Formal analysis. **Daniel A. Frick:** Methodology, Formal analysis. **Tommaso Di Rocco:** Formal analysis. **Moritz Liesegang:** Writing – review & editing, Investigation, Formal analysis. **Maria Stuff:** Investigation, Formal analysis. **Michael Wiedenbeck:** Writing – review & editing, Formal analysis.

Declaration of competing interest

The authors declare that they have no known competing financial interests or personal relationships that could have appeared to influence the work reported in this paper.

Data availability

Data will be made available on request.

Acknowledgements

We are grateful for funding of the field campaign through the DFG during FOR736 “The Precambrian–Cambrian Ecosphere (R)evolution: Insights from Chinese microcontinents” (grant no. BL 562/11-2). We thank Frédéric Couffignal for providing key support during the acquisition of SIMS data. Comments from two anonymous reviewers and V. Mavromatis are highly appreciated and helped to improve the clarity of the manuscript.

References

Abraham, K., Hofmann, A., Foley, S.F., Cardinal, D., Harris, C., Barth, M.G., André, L., 2011. Coupled silicon–oxygen isotope fractionation traces Archaean silicification. Earth Planet. Sci. Lett. 301, 222–230. Elsevier B.V.

Abruzzese, M.J., Waldbauer, J.R., Chamberlain, C.P., 2005. Oxygen and hydrogen isotope ratios in freshwater chert as indicators of ancient climate and hydrologic regime. Geochim. Cosmochim. Acta 69, 1377–1390.

Andrade, C.N., Chafetz, H.S., Lapen, T.J., 2020. Paragenesis of silicified mid-Paleozoic and mid-Cenozoic corals based on petrography and silicon isotopic analyses. Chem. Geol. 538, 119483. Elsevier.

Baertschi, P., 1976. Absolute 18O content of standard mean ocean water. Earth Planet. Sci. Lett. 31, 341–344.

Bustillo, M.A., 2010. Chapter 3 Silicification of Continental Carbonates. P. in: Developments in Sedimentology. Elsevier, 153–178 pp.

Chen, X., Chafetz, H.S., Andreasen, R., Lapen, T.J., 2016. Silicon isotope compositions of euhedral authigenic quartz crystals: Implications for abiotic fractionation at surface temperatures. Chem. Geol. 423, 61–73. Elsevier B.V.

Chen, K., Lü, X., Qian, Y., Wu, S., Dong, S., 2020. δ30Si and δ18O of Multiple Silica Phases in Chert: Implications for δ30Siseawater of Darriwilian Seawater and Sea Surface Temperatures. Palaeogeogr. Palaeoclimatol. Palaeoecol. 544.

Delstanche, S., Opfergelt, S., Cardinal, D., Elsass, F., André, L., Delvaux, B., 2009. Silicon isotopic fractionation during adsorption of aqueous monosilicic acid onto iron oxide. Geochim. Cosmochim. Acta 73, 923–934.

Ding, T., Wan, D., Bai, R., Zhang, Z., Shen, Y., Meng, R., 2005. Silicon isotope abundance ratios and atomic weights of NBS-28 and other reference materials. Geochim. Cosmochim. Acta 69, 5487–5494.

Ding, T.P., Gao, J.F., Tian, S.H., Fan, C.F., Zhao, Y., Wan, D.F., Zhou, J.X., 2017. The δ30Si peak value discovered in middle Proterozoic chert and its implication for environmental variations in the ancient ocean. Sci. Rep. 7, 44000. Nature Publishing Group.

Dupuis, R., Benoit, M., Nardin, E., Méheut, M., 2015. Fractionation of silicon isotopes in liquids: the importance of configurational disorder. Chem. Geol. 396, 239–254.

Eganov, E.A., Sovetov, Y.K., Yanshin, A.L., 1986. Cambrian, Proterozoic and phosphorite deposits: Karatau, southern Kazakhstan, USSR. In: Cook, P.J., Shergold, J.H. (Eds.), Phosphate Deposits of the World. Cambridge University Press, Cambridge, pp. 175–189.

Folk, R.L., Pittman, J.S., 1971. Length-slow Chalcedony: a New Testament for Vanished Evaporites. SEPM J. Sediment. Res. 41, 1045–1058.

Frick, D.A., Schuessler, J.A., von Blanckenburg, F., 2016. Development of routines for simultaneous in situ chemical composition and stable Si isotope ratios analyses by femtosecond laser ablation inductively coupled plasma mass spectrometry. Anal. Chim. Acta 938, 33–43. Elsevier Ltd.

Geilert, S., Vroon, P.Z., Roerdink, D.L., Van Cappellen, P., van Bergen, M.J., 2014a. Silicon isotope fractionation during abiotic silica precipitation at low temperatures: inferences from flow-through experiments. Geochim. Cosmochim. Acta 142, 95–114.

Geilert, S., Vroon, P.Z., van Bergen, M.J., 2014b. Silicon isotopes and trace elements in chert record early Archean basin evolution. Chem. Geol. 386, 133–142.

Geilert, S., Vroon, P.Z., Keller, N.S., Gudbrandsson, S., Stefánsson, A., van Bergen, M.J., 2015. Silicon isotope fractionation during silica precipitation from hot-spring

waters: evidence from the Geysir geothermal field, Iceland. Geochim. Cosmochim. Acta 164, 403–427.
Gunnarsson, I., Arnórsson, S., 2000. Amorphous silica solubility and the thermodynamic properties of H4SiO4° in the range of 0°to 350°C at P(sat). Geochim. Cosmochim. Acta 64, 2295–2307.
Guo, M., Wostbrock, J.A.G., Planavsky, N.J., Korenaga, J., 2022. Reconstructing seawater δ18O and D'17O values with solid Earth system Evolution. Earth Planet. Sci. Lett. 592, 117637. Elsevier B.V.
Hellmann, R., Wirth, R., Daval, D., Barnes, J.-P., Penisson, J.-M., Tisserand, D., Epicier, T., Florin, B., Hervig, R.L., 2012. Unifying natural and laboratory chemical weathering with interfacial dissolution–reprecipitation: a study based on the nanometer-scale chemistry of fluid–silicate interfaces. Chem. Geol. 294–295, 203–216. Elsevier B.V.
Hendry, K.R., Robinson, L.F., 2012. The relationship between silicon isotope fractionation in sponges and silicic acid concentration: Modern and core-top studies of biogenic opal. Geochim. Cosmochim. Acta 81, 1–12.
Hesse, R., 1989. Silica diagenesis: origin of inorganic and replacement cherts. Earth Sci. Rev. 26, 253–284.
Heubeck, C., Ergaliev, G., Evseev, S., 2013. Large-Scale Seismogenic Deformation of a Carbonate Platform Straddling the Precambrian–Cambrian Boundary, Karatau Range, Kazakhstan. J. Sediment. Res. 83, 1004–1024.
Hinman, N.W., 1990. Chemical factors influencing the rates and sequences of silica phase transitions : Effects of organic constituents. Geochim. Cosmochim. Acta 54, 1563–1574.
Hinman, N.W., 1998. Sequences of silica phase transitions: effects of Na, Mg, K, Al, and Fe ions. Mar. Geol. 147, 13–24.
IAEA, 1993. Reference and intercomparison Materials for Stable Isotopes of Light elements. Proceedings of a consultants meeting 1–165.
Ibarra, D.E., Yanchilina, A.G., Lloyd, M.K., Methner, K.A., Page Chamberlain, C., Yam, R., Shemesh, A., Stolper, D.A., 2022. Triple oxygen isotope systematics of diagenetic recrystallization of diatom opal-a to opal-CT to microquartz in deep sea sediments. In: Geochim. Cosmochim. Acta, 320, pp. 304–323.
Jochum, K.P., Nohl, U., Herwig, K., Lammel, E., Stoll, B., Hofmann, A.W., 2005. GeoReM: a New Geochemical Database for Reference Materials and Isotopic Standards. Geostand. Geoanal. Res. 29, 333–338.
Jochum, K.P., Weis, U., Stoll, B., Kuzmin, D., Yang, Q., Raczek, I., Jacob, D.E., Stracke, A., Birbaum, K., Frick, D.A., Günther, D., Enzweiler, J., 2011. Determination of reference values for NIST SRM 610-617 glasses following ISO guidelines. Geostand. Geoanal. Res. 35, 397–429.
Johnson, C.M., Beard, B.L., Albarède, F., 2004. Geochemistry on non-traditional stable isotopes. Rev. Mineral. Geochem. 1–24.
Kastner, M., Keene, J.B., Gieskes, J.M., 1977. Diagenesis of siliceous oozes-I. Chemical controls on the rate of opal-a to opal-CT transformation- an experimental study. Geochim. Cosmochim. Acta 41, 1041–1059.
Kelka, U., Veveakis, M., Koehn, D., Beaudoin, N., 2017. Zebra rocks: Compaction waves create ore deposits. Sci. Rep. 7, 1–9. Springer US.
Knauth, L.P., 1979. A model for the origin of chert in limestone. Geology 7, 274.
Knoll, A.H., 1985. Exceptional preservation of photosynthetic organisms in silicified carbonates and silicified peats. Philos. Trans. R. Soc. Lond. 311, 111–122.
Liesegang, M., Milke, R., Kranz, C., Neusser, G., 2017. Silica nanoparticle aggregation in calcite replacement reactions. Sci. Rep. 1–5. Springer US.
Liu, Y., Hu, Z., Gao, S., Günther, D., Xu, J., Gao, C., Chen, H., 2008. In situ analysis of major and trace elements of anhydrous minerals by LA-ICP-MS without applying an internal standard. Chem. Geol. 257, 34–43. Elsevier B.V.
Longerich, H.P., Jackson, S.E., Günther, D., 1996. Laser ablation inductively coupled plasma mass spectrometric transient signal data acquisition and analyte concentration calculation. J. Anal. At. Spectrom. 11, 899–904.
Maliva, R.G., Siever, R., 1987. Diagenetic replacement controlled by force of crystallization. Geology 16, 688–691.
Maliva, R.G., Siever, R., 1988. Mechanisms and controls of silicification of fossils in limestones. J. Geol. 96.
Maliva, R.G., Siever, R., 1989a. Chertification histories of some late Mesozoic and Middle Palaeozoic platform carbonates. Sedimentology 36, 907–926.
Maliva, R.G., Siever, R., 1989b. Nodular chert formation in carbonate rocks. J. Geol. 97, 421–433.
Maliva, R.G., Knoll, A.H., Siever, R., 1989. Secular Change in Chert distribution: a Reflection of Evolving Biological Participation in the Silica Cycle. Palaios 4, 519–532.
Maliva, R.G., Knoll, A.H., Simonson, B.M., 2005. Secular change in the Precambrian silica cycle: Insights from chert petrology. Geol. Soc. Am. Bull. 117, 835–845.
Marin-Carbonne, J., Robert, F., Chaussidon, M., 2014. The silicon and oxygen isotope compositions of Precambrian cherts: a record of oceanic paleo-temperatures? Precambrian Res. 247, 223–234.
Marshall, W.L., Warakomski, J.M., 1980. Amorphous silica solubilities-II. Effect of aqueous salt solutions at 25°C. Geochim. Cosmochim. Acta 44.
Murata, K.J., Friedman, I., Gleason, J.D., 1977. Oxygen isotope relations between diagenetic silica minerals in Monterey Shale, Temblor Range, California. Am. J. Sci. 277, 259–272.
National Institute of Standards and Technology, 2015. Report of Investigation, 1–3 pp.
Nielsen, P., Swennen, R., Muchez, P., Keppens, E., 1998. Origin of Dinantian zebra dolomites south of the Brabant-Wales Massif, Belgium. Sedimentology 45, 727–743.
Oelze, M., von Blanckenburg, F., Hoellen, D., Dietzel, M., Bouchez, J., 2014. Si stable isotope fractionation during adsorption and the competition between kinetic and equilibrium isotope fractionation: implications for weathering systems. Chem. Geol. 380, 161–171.
Oelze, M., von Blanckenburg, F., Bouchez, J., Hoellen, D., Dietzel, M., 2015. The effect of Al on Si isotope fractionation investigated by silica precipitation experiments. Chem. Geol. 397, 94–105. Elsevier B.V.
Pack, A., 2021. Isotopic traces of atmospheric O2 in rocks, minerals and melts. Rev. Mineral. Geochem. 217–240.
Pack, A., Tanaka, R., Hering, M., Sengupta, S., Peters, S., Nakamura, E., 2016. The oxygen isotope composition of San Carlos olivine on the VSMOW2-SLAP2 scale. Rapid Commun. Mass Spectrom. 1495–1504.
Papineau, D., Yin, J., Devine, K.G., Liu, D., She, Z., 2021. Chemically oscillating reactions during the diagenetic formation of ediacaran siliceous and carbonate botryoids. Minerals 11.
Pisani, L., Koltai, G., Dublyansky, Y., Kleine, B.I., Whitehouse, M.J., Skrzypek, E., Carbone, C., Spötl, C., Antonellini, M., Bezerra, F.H., De Waele, J., 2022. Hydrothermal silicification and hypogene dissolution of an exhumed Neoproterozoic carbonate sequence in Brazil: Insights from fluid inclusion microthermometry and silicon-oxygen isotopes. Basin Res. 1–26.
Pollington, A.D., Kozdon, R., Anovitz, L.M., Georg, R.B., Spicuzza, M.J., Valley, J.W., 2016. Experimental calibration of silicon and oxygen isotope fractionations between quartz and water at 250°C by in situ microanalysis of experimental products and application to zoned low δ30Si quartz overgrowths. Chem. Geol. 421, 127–142. Elsevier B.V.
Putnis, A., Putnis, C.V., 2007. The mechanism of reequilibration of solids in the presence of a fluid phase. J. Solid State Chem. 180, 1783–1786.
Racki, G., Cordey, F., 2000. Radiolarian palaeoecology and radiolarites: is the present the key to the past? Earth Sci. Rev. 52, 83–120.
Robert, F., Chaussidon, M., 2006. A palaeotemperature curve for the Precambrian oceans based on silicon isotopes in cherts. Nature 443, 969–972.
Roerdink, D.L., van den Boorn, S.H.J.M., Geilert, S., Vroon, P.Z., van Bergen, M.J., 2015. Experimental constraints on kinetic and equilibrium silicon isotope fractionation during the formation of non-biogenic chert deposits. Chem. Geol. 402, 40–51.
Schuessler, J.A., von Blanckenburg, F., 2014. Testing the limits of micro-scale analyses of Si stable isotopes by femtosecond laser ablation multicollector inductively coupled plasma mass spectrometry with application to rock weathering. Spectrochim. Acta B At. Spectrosc. 98, 1–18.
Sengupta, S., Peters, S.T.M., Reitner, J., Duda, J.P., Pack, A., 2020. Triple oxygen isotopes of cherts through time. Chem. Geol. 554, 119789. Elsevier.
Sharp, Z.D., 1990. A laser-based microanalytical method for the in situ determination of oxygen isotope ratios of silicates and oxides. Geochim. Cosmochim. 54, 1353–1357.
Sharp, Z.D., Gibbons, J.A., Maltsev, O., Atudorei, V., Pack, A., Sengupta, S., Shock, E.L., Knauth, L.P., 2016. A calibration of the triple oxygen isotope fractionation in the SiO2-H2O system and applications to natural samples. Geochim. Cosmochim. Acta 186, 105–119.
Siever, R., 1962. Silica solubility, 0°-200° C., and the diagenesis of siliceous sediments. J. Geol. 70, 127–150.
Siever, R., 1992. The silica cycle in the Precambrian. Geochim. Cosmochim. Acta 56, 3265–3272.
Stamm, F.M., Zambardi, T., Chmeleff, J., Schott, J., von Blanckenburg, F., Oelkers, E.H., 2019. The experimental determination of equilibrium Si isotope fractionation factors among H4SiO4o, H3SiO4− and amorphous silica (SiO2·0.32 H2O) at 25 and 75 °C using the three-isotope method. Geochim. Cosmochim. Acta 255, 49–68.
Steinhoefel, G., Breuer, J., von Blanckenburg, F., Horn, I., Sommer, M., 2017. The dynamics of Si cycling during weathering in two small catchments in the Black Forest (Germany) traced by Si isotopes. Chem. Geol. 466, 389–402. Elsevier.
Tatzel, M., von Blanckenburg, F., Oelze, M., Schuessler, J.A., Bohrmann, G., 2015. The silicon isotope record of early silica diagenesis. Earth Planet. Sci. Lett. 428, 293–303.
Tatzel, M., von Blanckenburg, F., Oelze, M., Bouchez, J., Hippler, D., 2017. Late Neoproterozoic seawater oxygenation by siliceous sponges. Nat. Commun. 8, 621. Springer US.
Tatzel, M., Stuff, M., Franz, G., Hippler, D., Wiechert, U., von Blanckenburg, F., 2020. Siliceous sponge expansion and phosphogenesis in a shallow water environment in the Malyi Karatau Range (Kazakhstan) during the Precambrian-Cambrian transition. Precambrian Res. 347.
Tatzel, M., Frings, P.J., Oelze, M., Herwartz, D., Lünsdorf, N.K., Wiedenbeck, M., 2022. Chert oxygen isotope ratios are driven by Earth's thermal evolution. Proc. Natl. Acad. Sci. 119.
Van Cappellen, P., Qiu, L., 1997a. Biogenic silica dissolution in sediments of the Southern Ocean, I. Solubility. Deep Sea Res. II 44, 1109–1128.
Van Cappellen, P., Qiu, L., 1997b. Biogenic silica dissolution in sediments of the Southern Ocean. II. Kinetics. Deep-Sea Res. II Top. Stud. Oceanogr. 44, 1129–1149.
van den Boorn, S.H.J.M., van Bergen, M.J., Nijman, W., Vroon, P.Z., 2007. Dual role of seawater and hydrothermal fluids in early Archean chert formation: evidence from silicon isotopes. Geology 35, 939.
van den Boorn, S.H.J.M., van Bergen, M.J., Vroon, P.Z., de Vries, S.T., Nijman, W., 2010. Silicon isotope and trace element constraints on the origin of ~3.5Ga cherts: Implications for early Archaean marine environments. Geochim. Cosmochim. Acta 74, 1077–1103. Elsevier Ltd.
Vandeginste, V., Swennen, R., Gleeson, S.A., Ellam, R.M., Osadetz, K., Roure, F., 2005. Zebra dolomitization as a result of focused fluid flow in the Rocky Mountains Fold and Thrust Belt, Canada. Sedimentology 52, 1067–1095.
Varkouhi, S., Papineau, D., 2023. Silica botryoids from chemically oscillating reactions and as Precambrian environmental proxies. Geology 51, 683–687.
von Blanckenburg, F., Wittmann, H., Schuessler, J.A., 2016. HELGES: Helmholtz Laboratory for the Geochemistry of the Earth Surface. J. Large Scale Res. Facilities 2, A84.
Wang, W., Geilert, S., Wei, H.-Z., Jiang, S.-Y., 2021. Competition of equilibrium and kinetic silicon isotope fractionation during silica precipitation from acidic to alkaline

pH solutions in geothermal systems. Geochim. Cosmochim. Acta 306, 44–62. Elsevier Ltd.
Wille, M., Sutton, J.N., Ellwood, M.J., Sambridge, M., Maher, W., Eggins, S., Kelly, M., 2010. Silicon isotopic fractionation in marine sponges: a new model for understanding silicon isotopic variations in sponges. Earth Planet. Sci. Lett. 292, 281–289.
Williams, L.A., Crerar, D.A., 1985. Silica diagenesis, II. General mechanisms. J. Sediment. Petrol. 55, 312–321.
Williams, L.A., Parks, G.A., Crerar, D.A., 1985. Silica Diagenesis, I. Solubility Controls. J. Sediment. Petrol. 55, 301–311.
Wostbrock, J.A.G., Sharp, Z.D., 2021. Triple oxygen isotopes in silica-water and carbonate-water systems. Triple Oxygen Isotope Geochem. 86, 367–400.
Wostbrock, J.A.G., Cano, E.J., Sharp, Z.D., 2020. An internally consistent triple oxygen isotope calibration of standards for silicates, carbonates and air relative to VSMOW2 and SLAP2. Chem. Geol. 533, 119432. Elsevier B.V.
Yanchilina, A.G., Yam, R., Kolodny, Y., Shemesh, A., 2020. From diatom opal-a δ18O to chert δ18O in deep sea sediments. Geochim. Cosmochim. Acta 268, 368–382. Elsevier Ltd.
Yanchilina, A.G., Yam, R., Shemesh, A., 2021. The effect of sediment lithology on oxygen isotope composition and phase transformation of marine biogenic opal. Chem. Geol. 570, 120175.
Young, E.D., Galy, A., Nagahara, H., 2002. Kinetic and equilibrium mass-dependant isotope fractionation laws in nature and their geochemical and cosmochemical significance. Geochim. Cosmochim. Acta 66, 1095–1104.
Zakharov, D.O., Marin-Carbonne, J., Alleon, J., Bindeman, I.N., 2021. Triple Oxygen Isotope Trend Recorded by Precambrian Cherts: a Perspective from combined Bulk and in situ secondary Ion Probe Measurements. Rev. Mineral. Geochem. 86, 323–365.
Zambardi, T., Poitrasson, F., 2011. Precise Determination of Silicon Isotopes in Silicate Rock Reference Materials by MC-ICP-MS. Geostand. Geoanal. Res. 35, 89–99.